Wetter East Asia and Western United States with projected delayed Southern Ocean warming

Hanjun Kim
hanjunkim0617@gmail.com

Cornell University
Sarah Kang
Max Planck Institute for Meteorology https://orcid.org/0000-0003-4635-275X
Angeline Pendergrass
Cornell University https://orcid.org/0000-0003-2542-1461
Flavio Lehner
Cornell University https://orcid.org/0000-0003-4632-9701
Yechul Shin
Seoul National University
Paulo Ceppi
Imperial College London https://orcid.org/0000-0002-3754-3506
Sang-Wook Yeh
swyeh@hanyang.ac.kr https://orcid.org/0000-0003-4549-1686
Se-Yong Song
Hanyang University https://orcid.org/0000-0002-9447-1158

Article

Keywords:

Posted Date: May 20th, 2024

DOI: https://doi.org/10.21203/rs.3.rs-4259688/v1

Additional Declarations: There is **NO** Competing Interest.

Wetter East Asia and Western United States with projected delayed Southern Ocean warming

Hanjun Kim[1*], Sarah M. Kang[2*], Angeline G. Pendergrass[1,3], Flavio Lehner[1,3],
Yechul Shin[4], Paulo Ceppi[5], Sang-Wook Yeh[6], Se-Yong Song[7]

[1]*Department of Earth and Atmospheric Sciences, Cornell University, Ithaca, NY, USA*
[2]*Max Planck Institute for Meteorology, Hamburg, Germany*
[3]*Climate and Global Dynamics Laboratory, National Center for Atmospheric Research, Boulder, CO, USA*
[4]*School of Earth and Environmental Sciences, Seoul National University, Seoul, South Korea*
[5]*Department of Physics, Imperial College London, London, United Kingdom*
[6]*Department of Marine Sciences and Convergent Technology, Hanyang University, ERICA, Ansan, South Korea*
[7]*Earth Research Institute, University of California Santa Barbara, Santa Barbara, CA, USA*

[*]*Corresponding author*: Hanjun Kim (hk764@cornell.edu) / Sarah M. Kang (Sarah.Kang@mpimet.mpg.de)

Abstract

Under global warming, precipitation over East Asia and the Western United States is projected to increase, though associated uncertainties are large. We argue that these precipitation enhancements are partly due to teleconnection from the Southern Ocean, which absorbs anthropogenic heat and gradually releases it with a delay. Based on climate model experiments, we show that the delayed Southern Ocean warming contributes to the tropical Pacific warming, enhancing precipitation during summer in East Asia and winter in the Western United States. An El Niño-like atmospheric teleconnection links the Southern Ocean warming to the Northern Hemisphere regional precipitation increases. Southern Hemisphere low clouds are a key regulator of this teleconnection, partly explaining the projected uncertainty of the regional precipitation. The documented teleconnection has practical implications: even if climate mitigation reduces carbon dioxide levels, the delayed Southern Ocean warming will sustain a wetter East Asia and Western United States for decades to centuries.

Main text

Effective adaptation to climate change hinges on accurate regional precipitation projections. This is particularly true for East Asia and the Western United States, regions with substantial precipitation variability and associated socio-economic impacts[1–3]. State-of-the-art climate models, however, show a high uncertainty of future precipitation changes in these regions[4]. The factor contributing to this uncertainty is inter-model differences in sea surface temperature (SST) projections over the tropical Pacific, reflecting an El Niño-like atmospheric teleconnections[5–9]. Climate models projecting a stronger El Niño-like warming pattern – stronger warming in the eastern equatorial Pacific compared to the western part – tend to exhibit a more pronounced precipitation increase in summer over East Asia[10] and winter over Western united States[11,12].

However, the underlying drivers of projection uncertainty in the tropical Pacific SST, and thus the regional precipitation, remain elusive. A key insight emerges from the common slow timescale shared by the tropical Pacific SST and regional precipitation responses. When CO_2 concentration is abruptly quadrupled in climate models, the eastern equatorial Pacific warming is initially muted but gradually evolves to an El Niño-like warming pattern[13,14] (Extended Data Fig. 1d). The regional precipitation over East Asia and Western United States also slowly increases following the slow timescale of the El Niño-like warming[15] (Extended Data Fig. 1e,f). Notably, the slowly emerging processes are the primary contributors to the multi-model mean and inter-model spread of the long-term responses (Extended Data Fig. 1g-i). This raises a critical question: What process in the slow timescale governs the uncertainty of the tropical Pacific warming and, consequently, the regional precipitation enhancements?

Building on these insights, we hypothesize that delayed warming of the Southern Ocean (SO) is a key slow process. Initially, ocean circulation over the SO mitigates SST warming by absorbing heat into the deep ocean. This ocean heat uptake gradually slows down and manifests as the delayed SO warming[16]. Meanwhile, the anomalous SO warming causes the tropical Pacific to warm particularly in the eastern basin, inducing the El Niño-like warming pattern, as revealed by recent idealized model experiments[17–20]. Here, through a series of climate model experiments, we demonstrate that the El Niño-like warming is partly attributable to the delayed SO warming. This SO warming, in turn, increases precipitation during summer in East Asia and winter in the Western United States, in both cases through El

Niño-like atmospheric teleconnections. We show that the Southern Hemisphere low cloud feedback modulates the entire teleconnection from the SO, partially explaining the inter-model spread of the regional precipitation projections over East Asia and the Western Unites States.

1. Tracing tropical Pacific warming back to the delayed Southern Ocean warming

The teleconnection from the delayed SO warming emerges in the slow response. In this study, we define the slow response as the difference between the last and the first 30 years of the 150-year CMIP6 abrupt4xCO2 simulation, in which CO_2 is abruptly quadrupled from pre-industrial levels[21] (Methods). In this section, we will focus on the remote impact the delayed SO warming has on the tropical Pacific SST, before investigating the impact on regional precipitation. The key cause of the inter-model differences in this entire teleconnection, the Southern Hemisphere low cloud feedback, will be introduced as well.

First, in the CMIP6 slow response of the SST, the warming is pronounced between 60°S-40°S, indicating the delayed SO warming (Fig. 1a). This is because the SO initially absorbs heat from the atmosphere but gradually releases it around 45 ° S (Supplementary Fig. 1). Meanwhile, the tropical Pacific warms with a triangular shape from the South Pacific (purple triangle in Fig. 1a), corresponding to the El Niño-like warming (Fig. 1e). To isolate the effect of the delayed SO warming, we conduct a numerical experiment with the CESM1-CAM4 fully coupled model, wherein a regional thermal forcing is applied between 40°S-60°S (Methods). The prescribed SO heating induces a response that resembles the CMIP6 slow response (compare Fig. 1b to 1a), with a high pattern correlation, 0.76 over the tropical Pacific between 30°S-30°N and 120°E-300°E. This resemblance implies that the tropical Pacific SST pattern of the slow response is contributed by the delayed SO warming.

The SO-driven teleconnection mechanism involves a tight coupling between the large-scale atmospheric circulation, coastal upwelling, and cloud radiative feedback[17–19,22–26]. In particular, the subtropical low cloud feedback is a key determinant of the teleconnection efficiency across different climate models, as a positive low cloud feedback amplifies the SST response in the subtropical Southeast Pacific and facilitates the equatorward propagation of the SST response[18,19]. Assuming the low cloud feedback's crucial role in regulating the teleconnections from the delayed SO warming, we examine whether the different low cloud feedback across models can explain the inter-model spread in the CMIP6 slow response. We first quantify the Southern Hemisphere low cloud feedback (CF_{SH}) as the sensitivity of SW cloud radiative effect to underlying SSTs averaged over the Southern Hemisphere regions with climatological low clouds[27], indicated by black boxes in Fig. 1c (Methods; Supplementary Fig. 2). Then, we regress the CMIP6 slow response against the CF_{SH} across different climate models (Fig. 1c). The regression map of the slow SST response suggests that the models with a stronger CF_{SH} exhibit a more enhanced triangular warming (purple triangle in Fig. 1a), with a significant inter-model correlation of 0.74 (Fig. 1f).

We further quantify the role of CF_{SH} from a regional cloud locking experiment. The abrupt4xCO2 simulation with the default CESM1-CAM5 is compared with a simulation wherein the cloud radiative feedbacks are disabled regionally over the climatological low cloud regions in the Southern Hemisphere (Supplementary Fig. 3; Methods). The differences of the slow response between the cloud-interactive and regional cloud-locked configurations represent the impact of CF_{SH} (Fig. 1d). It is evident that the CF_{SH} enhances the SO-driven teleconnection, as suggested by the similarity with the inter-model regression map (compare Fig. 1d to 1c). Indeed, the triangular warming and the El Niño-like warming are amplified with the interactive CF_{SH} relative to the cloud-locked experiments (green rectangles in Fig 1e). Put together, the Southern Hemisphere low cloud feedback modulates the SO-driven teleconnection, thereby regulating the slow response of the tropical Pacific SST pattern.

2. Remote impact on East Asian precipitation

The delayed SO warming further contributes to the slow precipitation increases in East Asia and the Western United States, via tropical SST anomalies and subsequent El Niño-like teleconnections. The Southern Hemisphere low cloud feedback, by modulating these teleconnections, contributes to the uncertainty in projections of precipitation at regional scales. In this section, we first focus on the precipitation over East Asia (EA; 25°N-40°N and 110°E-145°E) during the boreal summer months of June, July, and August (JJA).

The EA summer precipitation increases in both the CMIP6 slow response and the response to the SO warming alone (green boxes in Fig. 2a,b). Thus, the slow increase in the EA summer precipitation can be partly attributed to the delayed SO warming. In addition, the Southern Hemisphere low cloud feedback acts to amplify the EA precipitation increase, as confirmed by its inter-model regression onto the CF_{SH} (Fig. 2c) and the regional cloud locking experiment (Fig. 2d). Therefore, uncertainty in the Southern Hemisphere low cloud feedback will affect the EA summer precipitation.

An El Niño-like teleconnection provides the mechanism for this precipitation response. It has been previously shown that the equatorial Pacific warming enhances the EA summer precipitation via shifting the Asian jet southward, as in a typical El Niño year[6,9,28,29]. The mechanisms are described hereafter. First, the equatorial warming, driven by the delayed SO warming, leads to tropical upper-level warming following the moist adiabat (Fig. 3a). The resultant southward shift in the maximum meridional temperature gradient leads to the southward displacement of the Asian summer jet[28] (Fig. 3b). Indeed, the Asian jet shifts southward as warming from the SO increases (gray contours in Fig. 2a-d). The EA summer moistening is tightly linked to this southward jet shift among climate models (Fig. 2f). The tropical Pacific warming regulates the extent to which the Asian jet shifts southward (Fig. 2e), eventually modulating the EA summer precipitation (Fig. 2g). The EA summer precipitation enhancement is hence influenced by the tropical Pacific warming, which is in turn shaped by the delayed SO warming and the Southern Hemisphere low cloud feedback. Indeed, the entire teleconnection is modulated by the CF_{SH} within the cloud locking experiment (green rectangles in Fig. 2e-g).

We further reveal the dynamics of how the southward jet shift enhances EA summer precipitation. As the Asian jet shifts southward, the atmospheric column it passes through becomes shallower due to the elevated topography (Fig. 3b). Potential vorticity conservation implies a reduction in relative vorticity[30], and the subsequent anticyclonic flow triggered along the topography entails northerly wind downstream of the Tibetan Plateau[29] (Fig. 3c). Northerly anomalies result in moisture convergence within EA and thereby lead to the precipitation increase[6]. In addition, the southward shifted jet favors warm advection to EA in the mid-troposphere, as after the jet shift, the westerlies blow from the climatologically warmer regions over the Tibetan Plateau[31] (Fig. 3d). To balance the mid-tropospheric energy budget, the enhanced warm advection requires compensatory adiabatic cooling by anomalous upward motion (Supplementary Fig. 4). The anomalous upward motion enhances EA precipitation[32,33].

The aforementioned dynamics in the CMIP6 slow response can be consistently identified in the SO warming experiment as well (compare Fig. 3 to Extended Data Fig. 2). That is, the delayed SO warming causes the tropical Pacific warming, shifting the Asian jet southward, resulting in the anomalous northerly and mid-tropospheric warm advection east of the Tibetan Plateau, thereby increasing the EA precipitation. This teleconnection mechanism is stronger in climate models with stronger CF_{SH} (Extended Data Fig. 3). In addition, the interactive CF_{SH} amplifies the teleconnection mechanism, demonstrated by the cloud locking experiment (Extended Data Fig. 4). Therefore, the Southern Hemisphere low cloud feedback is partly responsible for the projection uncertainty in the EA summer moistening via an El Niño-like teleconnection.

3. Remote impact on precipitation around the United States

We now examine the slow CO_2-forced precipitation response in the Western United States (WUS; 30°N-45°N, 215°E-245°E) during the boreal winter months (December, January, February). The WUS precipitation increases in the CMIP6 slow response as well as in the SO warming experiment (green rectangles in Fig. 4a,b). In addition, the models with the stronger CF_{SH} exhibits more pronounced increase in the WUS precipitation (Fig. 4c). Consistently, the WUS precipitation increase is enhanced with the active CF_{SH}, implied by the cloud locking experiment (Fig. 4d). Hence, the slow increase in the WUS winter precipitation is attributed to the delayed SO warming and regulated by the Southern Hemisphere low cloud feedback.

Much like the EA precipitation enhancement, the WUS wetting is partly induced by an El Niño-like teleconnection, starting from the delayed SO warming. Previous research revealed that tropical Pacific warming induces low geopotential height anomalies reminiscent of the Pacific/North America pattern via Rossby wave responses, thereby enhancing winter precipitation over the WUS[5,11]. Indeed, in response to the amplified warming from the SO, the 200hPa geopotential height anomalies exhibit minima over the northeastern Pacific (gray contours in Fig. 4a-d), which resemble the Rossby wave responses in a typical El Niño year[34]. Models with stronger tropical Pacific warmings tend to have lower height anomalies (Fig. 4e), which further regulate the WUS precipitation response among models (Fig. 4f). As a result, the tropical Pacific warming influences the extent to which the WUS precipitation increases (Fig. 4g). The CF_{SH} mediates the strength of the tropical Pacific warming and hence modulates the entire teleconnection, as shown by the cloud locking experiment (green rectangles in Fig. 4e-g)

The dynamical mechanism by which the low height anomaly over the northeastern Pacific enhances the WUS precipitation is consistent with previous studies[5,35,36]. First, the low height anomaly formed by the Rossby wave response is barotropic and hence induces near-surface cyclonic flow over the northeastern Pacific (Fig. 5a). The cyclonic flow generates southwesterly winds directed towards the WUS, which in turn supply moisture and enhance precipitation. Second, the low height anomaly in the northeastern Pacific corresponds to the eastward extension of the Pacific jet, which would otherwise be concentrated in the western Pacific (Fig. 5b). Given that climatological storm track activity decreases from the Pacific to the WUS[35], this eastward jet extension steers more storms towards the WUS, thereby enhancing precipitation[36].

The dynamic mechanisms behind the WUS moistening are similar between the CMIP6 slow response and the SO warming experiment (Fig. 5a-d). The delayed SO warming induces a tropical Pacific warming, triggering a low geopotential height anomaly over the northeastern Pacific, increasing moisture supply and changing the storm track, thereby intensifying the precipitation over the WUS. The Southern Hemisphere low cloud feedback amplifies these dynamic changes, as demonstrated by the inter-model regression and the cloud locking experiment (Fig. 5e-h). Likewise, this El Niño-like teleconnection propagates the uncertainty of the diverging CF_{SH} among models to the WUS winter precipitation.

The slow precipitation increase in the Southeastern United States (SEUS) is also partly explained by the SO-driven teleconnection. The SEUS precipitation during winter increases with the warming from the SO (green parallelograms in Fig. 4a-d). The tropical Pacific warming induces low height anomalies over the SEUS (gray contours in Fig. 4a-d), thereby increasing the SEUS rainfall as in El Niño years[37]. This El Niño-like teleconnection is further confirmed by the inter-model correlation between the tropical Pacific warming, low-height anomaly, and the SEUS precipitation increase (Extended Data Fig. 5). The CF_{SH} amplifies the circulation response favorable for a wetter SEUS, as shown by the inter-model regression and the cloud locking experiment (Fig. 5e-h). Therefore, the Southern Hemisphere low cloud feedback is partly responsible for the projection uncertainty in the SEUS precipitation as well.

Our analysis concentrated on the slow climate response to abrupt CO_2 quadrupling, specifically the gradual evolution of the tropical Pacific warming and related changes in regional precipitation. These slow responses dominate the long-term responses in the same scenario, as shown in Extended Data Fig. 1. Consistently, the Southern Hemisphere low cloud feedback explains the projection uncertainties not only for the slow responses but also for the long-term responses (Extended Data Fig. 6). While the inter-model correlation is dominated by four CESM2 variant models, the cloud locking experiment aligns with the inter-model relationship (compare black regression lines and green dashed lines in Extended Data Fig. 6). Given that the cloud locking experiment provides actual causal evidence, whereas the inter-model correlation does not, we argue that the CF_{SH} is partly responsible for the inter-model spread, even amidst the non-robust inter-model correlation. Thus, under the scenario with CO_2 enhancements, the misrepresentation of low clouds in the Southern Hemisphere will contribute to the projection uncertainties of tropical SSTs and regional precipitation changes over EA, WUS, and SEUS.

Discussion

Here, we reveal a teleconnection in which the delayed SO warming expected under anthropogenic climate change contributes to tropical Pacific warming, thereby enhancing regional precipitation over East Asia, the Western Unites States, and the Southeastern United States. The Southern Hemisphere low cloud feedback regulates the strength of the SO-driven teleconnection and partly explains the inter-model uncertainties of the regional precipitation projections. In fact, the highly model-dependent feedback from the Southern Hemisphere low clouds has been identified as a major source of uncertainty in global mean temperature increase and thus climate sensitivity[38–40]. Therefore, recent field campaigns focusing on the Southern Hemisphere low cloud[41,42] will prove valuable to improve not only climate sensitivity estimates but also regional precipitation projections.

In response to global warming, the slow teleconnections we describe here occur on centennial timescales as the SO slowly absorbs and releases heat, implying less impact on the near-future transient climate. However, the teleconnection impact will be more evident as humans reduce GHGs; the SO warming will persist while other regions will cool or equilibrate faster due to the differing heat capacities[43]. Indeed, in recent climate model experiments in which CO_2 is removed after transient quadrupling, the SO warming becomes pronounced when CO_2 is removed (Fig. 6c-d). The SO warming sustains the enhanced tropical Pacific warming, inducing dynamical changes identical to this study, thereby sustaining precipitation increase over the East Asia, Western United States, and the Southeastern United States (Fig. 6e-h).

This sustained warming and wetting is consistent with recent studies with similar model experiments[44,45]. Eventually, long-term adaptation policies need to reflect these regional climate changes induced by the SO warming, which will remain even with CO_2 reductions.

Generally, there is growing evidence indicating that the SO is a global climate pacemaker in recent trends, producing remote impacts such as those highlighted in this study[46–48]. Specifically, in the process of developing decadal climate predictions, higher spatial resolution was shown to improve the prediction skill of surface temperature over the SO. This SO skill improvement extends to a better hindcast of the tropical Pacific SST as well as the WUS and SEUS precipitation during winter[48]. Therefore, an accurate representation of recent SO cooling trends may play a crucial role in resolving model-observation discrepancies of the recent tropical Pacific cooling as well as the WUS drying. The mechanisms revealed in this study lend further support to this hypothesis. These cumulative findings could help alleviate model errors in simulating recent regional precipitation trends and enable more trustworthy future projections.

Methods

CMIP analysis

We use monthly-mean outputs of two fully-coupled CMIP6[21] experiments: piControl and abrupt4xCO2. piControl mimics the climate with pre-industrial CO_2 concentration (280ppm) and abrupt4xCO2 simulates the climate with quadrupled CO_2. We calculate the total response to CO_2 quadrupling as the difference between the last 30 years of abrupt4xCO2 and the last 100 years of piControl. We calculate the slow response as the last minus first 30 years of abrupt4xCO2, in which the effect of ocean dynamics and slowly evolving SSTs dominate. While previous studies used the first 10 years to capture the slow evolution of the SST, here we use the first 30 years to minimize the high internal variability in regional precipitation. We mainly focus on the slow response since the delayed SO heat release becomes evident only on this slow timescale (Supplementary Fig. 1b). All CMIP6 data are interpolated to 1°x1° horizontal resolution and one ensemble per model is used for the analysis. A total of 35 models are selected based on their data availability (model lists are provided in Supplementary Table 1).

The SO warming experiment using CESM1-CAM4

To confirm the SO-driven teleconnection impact, a SO warming experiment is conducted using the fully coupled CESM1-CAM4[49]. We first equilibrate to the pre-industrial climate and then add the SO warming. The target warming is added to the longwave heat flux term in the ocean coupler code. We add a sinusoidal heat flux between 40°S-60°S, with a maximum of 20 W m^{-2}. The averaged difference between the last 50 years of forced climate and last 100 years of pre-industrial climate is analyzed. The imposed heat flux is eventually released toward the atmosphere (dashed-dotted blue line in Supplementary Fig.1b), affecting the global climate through teleconnections. Note that the tropical Pacific response in this experiment is weaker than those in the CMIP6 slow response, even if the forcing magnitude is larger (Fig. 1a,b). The weaker response can be attributed to the too low stratocumulus cloud feedback strength in CESM1-CAM4[18], which would dampen the teleconnection impact in this particular model relative to most CMIP models.

Estimating Southern Hemisphere low cloud feedback

In this study, we aim to find the cause of the inter-model spread in the SW cloud radiative effect (SWCRE) responses over the Southern Hemisphere low cloud regions. We decompose the SWCRE response as the product of the forced SST response and the SWCRE sensitivity to SST, a relationship that holds particularly for the low cloud regions[19,39]. The SWCRE sensitivity at each grid point is the estimated strength of the local SW cloud feedback, which would be intrinsic to model's parameterizations.

We calculate the local SW cloud feedback strength by regressing the monthly SWCRE at Top-Of-Atmosphere (TOA) onto the monthly SST at each model grid point, using the de-seasonalized and de-trended deviations of 100-year piControl simulations. Then, the local SW cloud feedback is averaged over the Southern Hemisphere low cloud regions, where the inter-model correlation between the SWCRE changes and the tropical Pacific triangular warming is large (green and blue boxes in Supplementary Fig. 2a,b). The averaged feedback is what we refer to as the Southern Hemisphere low cloud feedback (CF_{SH}). This low cloud feedback can explain the inter-model spread of SWCRE changes both in the subtropical and SO domains even without considering the SST changes (Supplementary Fig. 2d-e). This indicates that the difference in low cloud parameterization is the dominant cause of the inter-model spread in the SWCRE responses. We estimate observational CF_{SH} with the same method, using the CERES-EBAF[50] for SWCRE and OISSTv5[51] for SST from March 2000 to February 2020.

Here, the Southern Hemisphere low cloud includes the cloud over the subtropics and SO, and the subtropical and SO cloud feedbacks are correlated among climate models (r=0.63; Supplementary Fig. 2c). In addition, note that we directly link the low cloud and SWCRE changes to the SST. In previous studies using cloud-controlling factor analysis, estimated inversion strength is another important factor for explaining SWCRE changes[39,52,53]. However, for the Southern Hemisphere low cloud regions, the anti-correlation between the inter-annual SST and estimated inversion strength is strong (not shown), hence the univariate regression with SST is sufficient to capture the inter-model spread of SWCRE responses.

The CESM1-CAM5 regional cloud locking experiment

To elucidate the role of CF_{SH}, we conduct regional cloud locking experiments using the fully coupled CESM1-CAM5[54–56]. First, the eight cloud parameters are extracted every 2 hours from a randomly chosen year of the equilibrated pre-industrial simulation. Then, in the regional cloud locking experiments, the 2-hourly cloud parameters are prescribed repetitively every year in the radiative transfer code for the target region. The target regions we focus on are the SO and off the west coast of all major Southern Hemisphere continents, where CF_{SH} is defined. One abrupt4xCO2 simulation is integrated for 150 years with the interactive clouds and the locked clouds. The effect is that the SW cloud radiative forcing in interactive cloud experiment is muted in the regionally locked experiment (Supplementary Fig. 3). The difference between the interactive and locked cloud experiment elucidates the role of the CF_{SH}; the slow response is used for the analysis as in CMIP.

Tropical SST pattern and the geopotential height pattern

The tropical SST pattern is calculated as the SST from which the tropical (20°S–20°N) mean has been subtracted. For the 200hPa and 850hPa geopotential height pattern, the deviation from the Northern Hemisphere (0°–40°N) average value is used to capture the circulation responses under global warming, following the previous study[57].

Asian jet shift

The shift of the Asian summer jet is quantified as the change in meridional asymmetry of the 200hPa zonal wind as follows. First, we take the 200hPa zonal wind during the summer (JJA) over the Asian continent (60°E–120°E). Next, we calculate the climatological Asian jet position as the latitude of the maximum zonally averaged zonal wind. To assess the meridional asymmetry of zonal wind (U200asy), the meridionally-averaged zonal wind between the climatological jet position and 20° south of the jet is subtracted from that between the climatological jet and 20° north of the jet. Negative changes in $U200_{asy}$ denote a southward shift in the Asian summer jet.

References

1. Zhang, W. *et al.* Increasing precipitation variability on daily-to-multiyear time scales in a warmer world. *Sci. Adv.* **7**, eabf8021 (2021).
2. World Meteorological Organization (WMO). *State of the Climate in Asia 2022*. https://wmo.int/publication-series/state-of-climate-asia-2022 (2023).
3. NOAA National Centers for Environmental Information (NCEI). *U.S. Billion-Dollar Weather and Climate Disasters*. https://www.ncei.noaa.gov/access/billions/, DOI: 10.25921/stkw-7w73 (2024).
4. Intergovernmental Panel On Climate Change. *Climate Change 2021 – The Physical Science Basis: Working Group I Contribution to the Sixth Assessment Report of the Intergovernmental Panel on Climate Change*. (Cambridge University Press, 2023). doi:10.1017/9781009157896.
5. Allen, R. J. & Luptowitz, R. El Niño-like teleconnection increases California precipitation in response to warming. *Nat Commun* **8**, 16055 (2017).
6. Chiang, J. C. H., Fischer, J., Kong, W. & Herman, M. J. Intensification of the Pre-Meiyu Rainband in the Late 21st Century. *Geophysical Research Letters* **46**, 7536–7545 (2019).
7. Trenberth, K. E. *et al.* Progress during TOGA in understanding and modeling global teleconnections associated with tropical sea surface temperatures. *J. Geophys. Res.* **103**, 14291–14324 (1998).
8. Yeh, S.-W. *et al.* ENSO Atmospheric Teleconnections and Their Response to Greenhouse Gas Forcing. *Rev. Geophys.* **56**, 185–206 (2018).
9. Zhou, W., Xie, S.-P. & Yang, D. Enhanced equatorial warming causes deep-tropical contraction and subtropical monsoon shift. *Nat. Clim. Chang.* **9**, 834–839 (2019).
10. He, C. & Zhou, T. Responses of the Western North Pacific Subtropical High to Global Warming under RCP4.5 and RCP8.5 Scenarios Projected by 33 CMIP5 Models: The Dominance of Tropical Indian Ocean–Tropical Western Pacific SST Gradient. *Journal of Climate* **28**, 365–380 (2015).
11. Dong, L., Leung, L. R., Song, F. & Lu, J. Uncertainty in El Niño-like warming and California precipitation changes linked by the Interdecadal Pacific Oscillation. *Nat Commun* **12**, 6484 (2021).
12. Dong, L. & Leung, L. R. Winter Precipitation Changes in California Under Global Warming:

Contributions of CO_2, Uniform SST Warming, and SST Change Patterns. *Geophys Res Lett* **48**, (2021).

13. Heede, U. K., Fedorov, A. V. & Burls, N. J. Time Scales and Mechanisms for the Tropical Pacific Response to Global Warming: A Tug of War between the Ocean Thermostat and Weaker Walker. *Journal of Climate* **33**, 6101–6118 (2020).
14. Heede, U. K. & Fedorov, A. V. Eastern equatorial Pacific warming delayed by aerosols and thermostat response to CO2 increase. *Nat. Clim. Chang.* **11**, 696–703 (2021).
15. Zappa, G., Ceppi, P. & Shepherd, T. G. Time-evolving sea-surface warming patterns modulate the climate change response of subtropical precipitation over land. *Proc. Natl. Acad. Sci. U.S.A.* **117**, 4539–4545 (2020).
16. Armour, K. C., Marshall, J., Scott, J. R., Donohoe, A. & Newsom, E. R. Southern Ocean warming delayed by circumpolar upwelling and equatorward transport. *Nature Geosci* **9**, 549–554 (2016).
17. Hwang, Y.-T., Xie, S.-P., Deser, C. & Kang, S. M. Connecting tropical climate change with Southern Ocean heat uptake: Tropical Climate Change and SO Heat Uptake. *Geophys. Res. Lett.* **44**, 9449–9457 (2017).
18. Kim, H., Kang, S. M., Kay, J. E. & Xie, S.-P. Subtropical clouds key to Southern Ocean teleconnections to the tropical Pacific. *Proc. Natl. Acad. Sci. U.S.A.* **119**, e2200514119 (2022).
19. Mechoso, C. R. *et al.* Can reducing the incoming energy flux over the Southern Ocean in a CGCM improve its simulation of tropical climate?: Southern Ocean-Tropics Link in a CGCM. *Geophys. Res. Lett.* **43**, 11,057-11,063 (2016).
20. Xiang, B., Zhao, M., Ming, Y., Yu, W. & Kang, S. M. Contrasting Impacts of Radiative Forcing in the Southern Ocean versus Southern Tropics on ITCZ Position and Energy Transport in One GFDL Climate Model. *Journal of Climate* **31**, 5609–5628 (2018).
21. Eyring, V. *et al.* Overview of the Coupled Model Intercomparison Project Phase 6 (CMIP6) experimental design and organization. *Geosci. Model Dev.* **9**, 1937–1958 (2016).
22. Kang, S. M. *et al.* Walker circulation response to extratropical radiative forcing. *Sci. Adv.* **6**, eabd3021 (2020).

23. Hwang, Y.-T. *et al.* Relative Roles of Energy and Momentum Fluxes in the Tropical Response to Extratropical Thermal Forcing. *Journal of Climate* **34**, 3771–3786 (2021).

24. Shin, Y. *et al.* Evolution of the Tropical Response to Periodic Extratropical Thermal Forcing. *Journal of Climate* 1–53 (2021) doi:10.1175/JCLI-D-20-0493.1.

25. Dong, Y., Armour, K. C., Battisti, D. S. & Blanchard-Wrigglesworth, E. Two-Way Teleconnections between the Southern Ocean and the Tropical Pacific via a Dynamic Feedback. *Journal of Climate* **35**, 6267–6282 (2022).

26. England, M. R., Polvani, L. M., Sun, L. & Deser, C. Tropical climate responses to projected Arctic and Antarctic sea-ice loss. *Nat. Geosci.* **13**, 275–281 (2020).

27. Myers, T. A. *et al.* Observational constraints on low cloud feedback reduce uncertainty of climate sensitivity. *Nat. Clim. Chang.* **11**, 501–507 (2021).

28. Zhou, W., Leung, L. R. & Lu, J. Seasonally and Regionally Dependent Shifts of the Atmospheric Westerly Jets under Global Warming. *Journal of Climate* **35**, 5433–5447 (2022).

29. Kong, W. & Chiang, J. C. H. Southward Shift of Westerlies Intensifies the East Asian Early Summer Rainband Following El Niño. *Geophysical Research Letters* **47**, (2020).

30. Holton, J. R. *An Introduction to Dynamic Meteorology*. (Elsevier Science, 2004).

31. Boos, W. R. & Kuang, Z. Dominant control of the South Asian monsoon by orographic insulation versus plateau heating. *Nature* **463**, 218–222 (2010).

32. Chen, J. & Bordoni, S. Early Summer Response of the East Asian Summer Monsoon to Atmospheric CO2 Forcing and Subsequent Sea Surface Warming. *Journal of Climate* **29**, 5431–5446 (2016).

33. Sampe, T. & Xie, S.-P. Large-Scale Dynamics of the Meiyu-Baiu Rainband: Environmental Forcing by the Westerly Jet*. *Journal of Climate* **23**, 113–134 (2010).

34. Horel, J. D. & Wallace, J. M. Planetary-Scale Atmospheric Phenomena Associated with the Southern Oscillation. *Monthly Weather Review* **109**, 813–829 (1981).

35. Chang, E. K. M., Zheng, C., Lanigan, P., Yau, A. M. W. & Neelin, J. D. Significant modulation of variability and projected change in California winter precipitation by extratropical cyclone activity:

CALIFORNIA PRECIPITATION AND CYCLONES. *Geophys. Res. Lett.* **42**, 5983–5991 (2015).

36. Neelin, J. D., Langenbrunner, B., Meyerson, J. E., Hall, A. & Berg, N. California Winter Precipitation Change under Global Warming in the Coupled Model Intercomparison Project Phase 5 Ensemble. *Journal of Climate* **26**, 6238–6256 (2013).
37. Ropelewski, C. F. & Halpert, M. S. North American Precipitation and Temperature Patterns Associated with the El Niño/Southern Oscillation (ENSO). *Monthly Weather Review* **114**, 2352–2362 (1986).
38. Zelinka, M. D. *et al.* Causes of Higher Climate Sensitivity in CMIP6 Models. *Geophys. Res. Lett.* **47**, (2020).
39. Brient, F. & Schneider, T. Constraints on Climate Sensitivity from Space-Based Measurements of Low-Cloud Reflection. *Journal of Climate* **29**, 5821–5835 (2016).
40. Tan, I., Storelvmo, T. & Zelinka, M. D. Observational constraints on mixed-phase clouds imply higher climate sensitivity. *Science* **352**, 224–227 (2016).
41. McFarquhar, G. M. *et al.* Observations of Clouds, Aerosols, Precipitation, and Surface Radiation over the Southern Ocean: An Overview of CAPRICORN, MARCUS, MICRE, and SOCRATES. *Bulletin of the American Meteorological Society* **102**, E894–E928 (2021).
42. Mechoso, C. R. *et al.* Ocean–Cloud–Atmosphere–Land Interactions in the Southeastern Pacific: The VOCALS Program. *Bulletin of the American Meteorological Society* **95**, 357–375 (2014).
43. Kim, S.-K. *et al.* Widespread irreversible changes in surface temperature and precipitation in response to CO2 forcing. *Nat. Clim. Chang.* **12**, 834–840 (2022).
44. Kug, J.-S. *et al.* Hysteresis of the intertropical convergence zone to CO2 forcing. *Nat. Clim. Chang.* **12**, 47–53 (2022).
45. Song, S.-Y. *et al.* Asymmetrical response of summer rainfall in East Asia to CO2 forcing. *Science Bulletin* **67**, 213–222 (2022).
46. Kang, S. M., Ceppi, P., Yu, Y. & Kang, I.-S. Recent global climate feedback controlled by Southern Ocean cooling. *Nat. Geosci.* **16**, 775–780 (2023).
47. Kang, S. M. *et al.* Global impacts of recent Southern Ocean cooling. *Proc. Natl. Acad. Sci. U.S.A.* **120**,

e2300881120 (2023).

48. Yeager, S. G. *et al.* Reduced Southern Ocean warming enhances global skill and signal-to-noise in an eddy-resolving decadal prediction system. *npj Clim Atmos Sci* **6**, 107 (2023).
49. Gent, P. R. *et al.* The Community Climate System Model Version 4. *J. Climate* **24**, 4973–4991 (2011).
50. Loeb, N. G. *et al.* Clouds and the Earth's Radiant Energy System (CERES) Energy Balanced and Filled (EBAF) Top-of-Atmosphere (TOA) Edition-4.0 Data Product. *J. Climate* **31**, 895–918 (2018).
51. Reynolds, R. W., Rayner, N. A., Smith, T. M., Stokes, D. C. & Wang, W. An Improved In Situ and Satellite SST Analysis for Climate. *J. Climate* **15**, 1609–1625 (2002).
52. Qu, X., Hall, A., Klein, S. A. & Caldwell, P. M. On the spread of changes in marine low cloud cover in climate model simulations of the 21st century. *Clim Dyn* **42**, 2603–2626 (2014).
53. Ceppi, P. & Nowack, P. Observational evidence that cloud feedback amplifies global warming. *Proc. Natl. Acad. Sci. U.S.A.* **118**, e2026290118 (2021).
54. Hurrell, J. W., Holland, M. M. & Gent, P. R. THE COMMUNITY EARTH SYSTEM MODEL. 23.
55. Middlemas, E. A., Clement, A. C., Medeiros, B. & Kirtman, B. Cloud Radiative Feedbacks and El Niño–Southern Oscillation. *Journal of Climate* **32**, 4661–4680 (2019).
56. Middlemas, E. A., Kay, J. E., Medeiros, B. M. & Maroon, E. A. Quantifying the Influence of Cloud Radiative Feedbacks on Arctic Surface Warming Using Cloud Locking in an Earth System Model. *Geophys. Res. Lett.* **47**, (2020).
57. He, C. *et al.* Enhanced or Weakened Western North Pacific Subtropical High under Global Warming? *Sci Rep* **5**, 16771 (2015).

Data availability

CMIP6 data are available from the ESGF data portals (https://esgf-node.llnl.gov/projects/esgf-llnl/). The post-processed CESM1-CAM4 Southern Ocean warming experiment and CESM1-CAM5 regional cloud locking experiment are available at https://zenodo.org/records/10866689. The observational SST (OISST v2) can be downloaded from Physical Sciences Laboratory website (https://psl.noaa.gov/data/gridded/data.noaa.oisst.v2.html). The CERES-EBAF v4.1 TOA radiation data are available from https://ceres.larc.nasa.gov/data/.

Code availability

The raw data are first averaged and interpolated by NetCDF Operator (NCO; https://nco.sourceforge.net/). All calculations, analysis, and visualizations were then carried out using MATLAB. The MATLAB codes are available at https://doi.org/10.5281/zenodo.10866689.

Acknowledgements

H.K. and F. L. are supported by NOAA MAPP award NA21OAR4310349. H.K. and S.M.K. have been supported by the Research Program for the carbon cycle between oceans, land, and atmosphere of the National Research Foundation (NRF) funded by the Ministry of Science and ICT (NRF-2022M3I6A1090965). The authors want to express special thanks to the developer of Synda Transfer Module, which is used for downloading CMIP data (https://espri-mod.github.io/synda/index.html).

Author Contributions

H.K. and S.M.K. conceived the study and designed the experiments. H.K did the analysis and wrote a first draft. H.K., Y.S., and S.S. performed modeling experiments. H.K., A.P., and F.L. analyze the teleconnection mechanisms in detail. All authors contributed to discussions of the results and revisions of the manuscript.

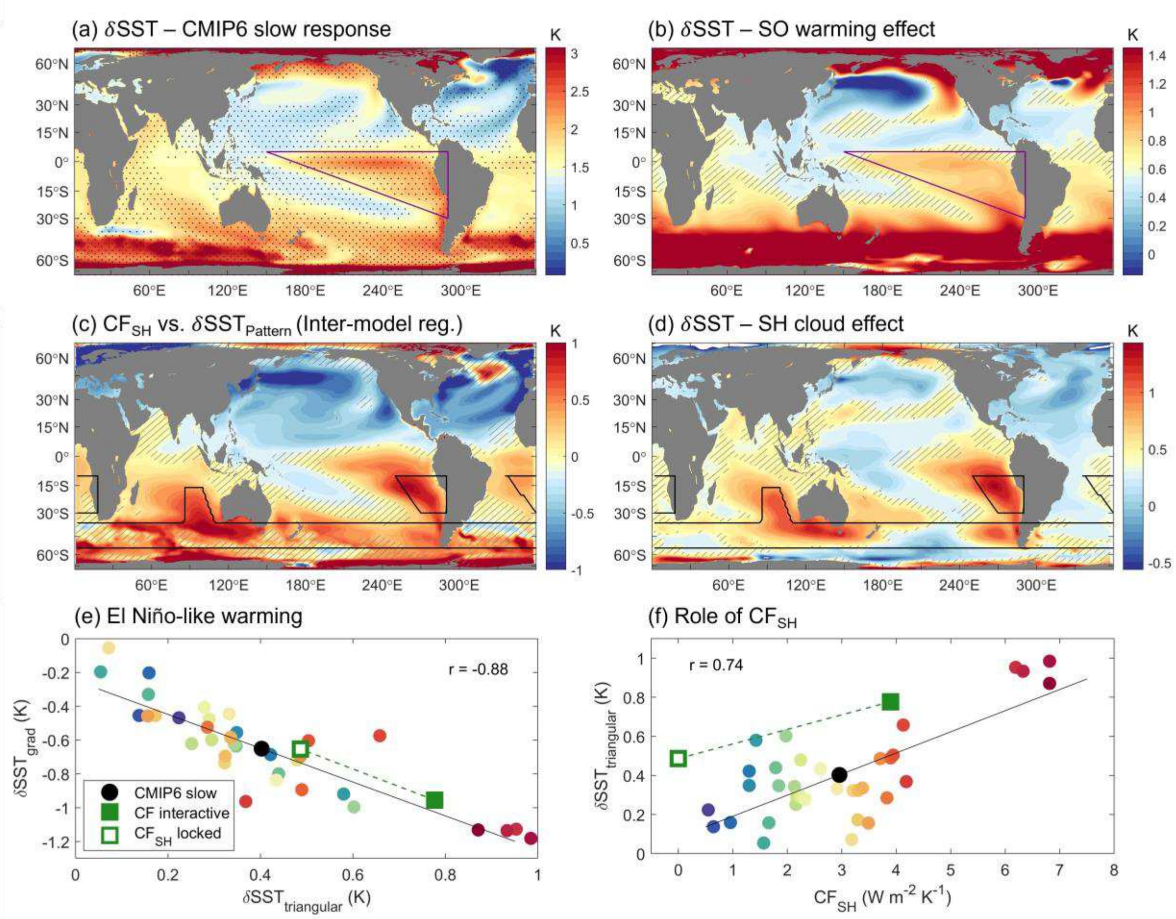

Fig. 1| Southern Ocean-to-tropics teleconnection and role of the Southern Hemisphere low cloud feedback (CF_{SH}). a-d, Annual mean SST from (**a**) multi-model mean CMIP6 slow response to CO_2 quadrupling, (**b**) CESM1-CAM4 SO warming experiment, (**c**) inter-model regression of CMIP6 slow response onto the CF_{SH}, and (**d**) CESM1-CAM5 regional cloud locking experiment. Note that tropical SST pattern (Methods) is used for the inter-model regression in (c) and the tropical mean SST is used as the center of color scale in (a,b,d). Stippling in (a) indicates where >70% of 35 models agree on the sign of pattern change. Unhatched shading in (b-d) indicates statistically significant signals at the 95% level using a *t* test. **e,** Tropical Pacific triangular warming versus equatorial Pacific SST gradient changes. The triangular warming is averaged over the purple triangle in (a), using the tropical SST pattern. The SST gradient is the difference of the west (80°E-150°E) minus east (210°E-280°E) near the equator (5°S-5°N). **f**, Relationship between the CF_{SH} and the tropical Pacific triangular warming. Circles indicate CMIP6 slow response, color-coded from blue to red in ascending order of the CF_{SH}. Black circle is multi-model mean and inter-model correlation is inserted as text. Empty (filled) green rectangle indicates CESM1-CAM5 experiment in which the clouds are regionally locked (globally interactive).

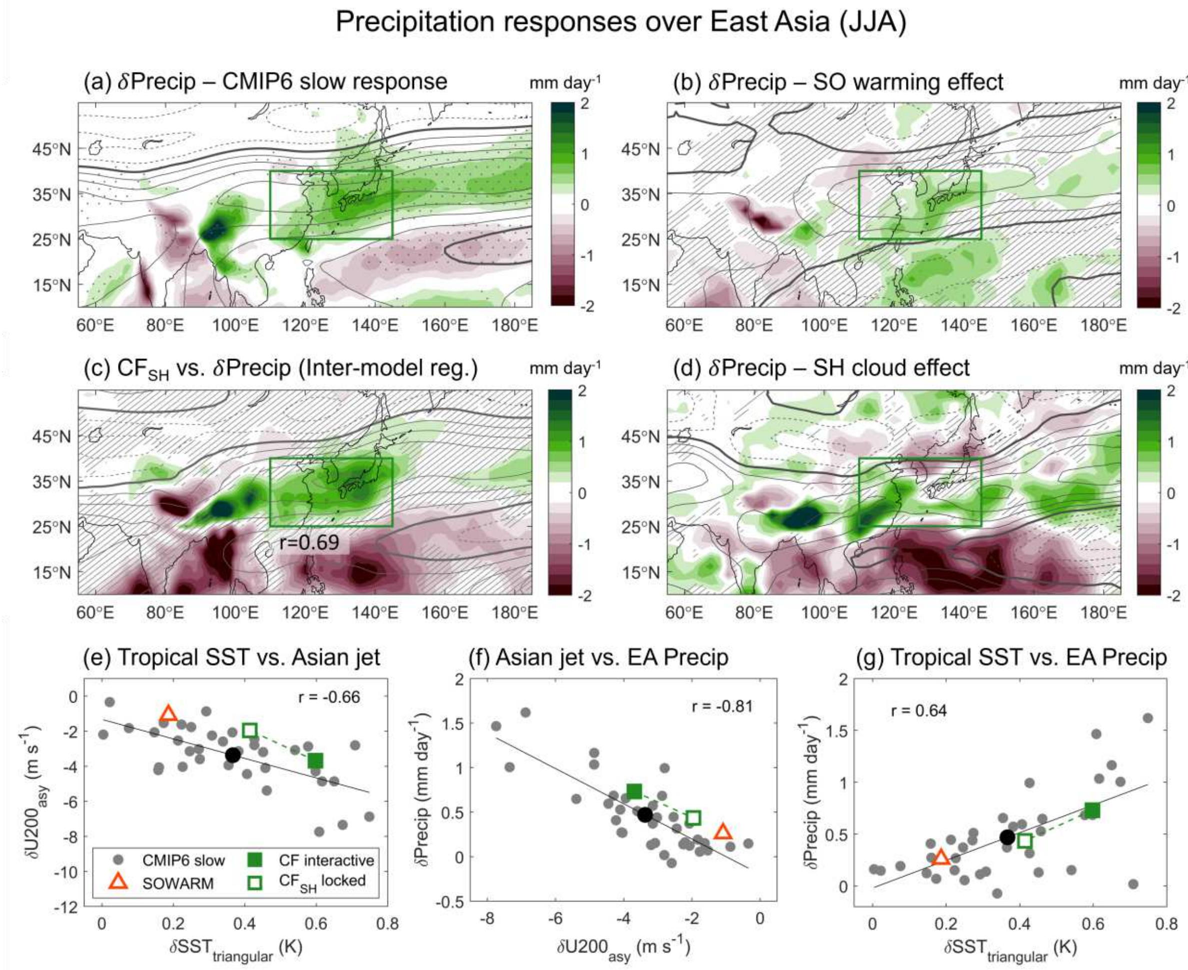

Fig. 2| Remote impact on the East Asia summer (JJA) precipitation. a-d, Precipitation (shading) and 200hPa zonal wind (contours) from (**a**) multi-model mean CMIP6 slow response, (**b**) CESM1-CAM4 SO warming experiment, (**c**) inter-model regression of CMIP6 slow response onto the CF_{SH}, and (**d**) CESM1-CAM5 regional cloud locking experiment. The solid (dashed) gray contours represent positive (negative) anomalies (interval = 0.8 m s^{-1}), where the thick line specifies zero. Stippled and unhatched regions indicate the statistical significance as in Figs. 1a-d. **e-g,** Relationship between (**e**) the tropical Pacific triangular warming and the Asian jet shift, (**f**) the Asian jet shift and the EA precipitation changes, and (**g**) the triangular warming and the EA precipitation changes. The Asian jet shift is measured by changes in meridional asymmetry of 200hPa zonal wind, in which negative sign indicates southward shift (Method). The EA precipitation is averaged over the green boxes in (a-d). Circle symbols are CMIP6 slow responses, black is multi-model mean. Orange triangles indicate the CESM1-CAM4 SO warming experiment. The empty (filled) green rectangle indicates the CESM1-CAM5 experiment in which the clouds are regionally locked (globally interactive).

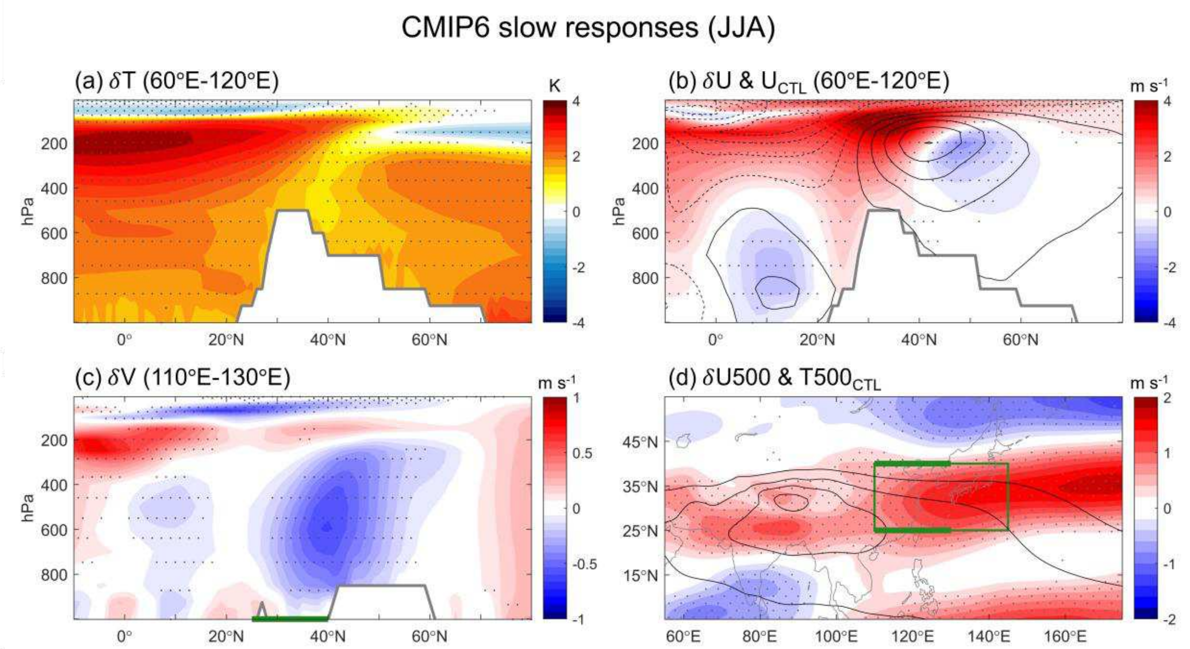

Fig. 3| The El Niño-like teleconnection to East Asia in multi-model mean CMIP6 slow response. a, Response in vertical temperature profile averaged over the Asian sector (60°E - 120°E). **b,** Response (shading) and climatology (contours; interval = 6 m s^{-1}) of the vertical profile of zonal wind over the Asian sector (60°E-120°E). The solid (dashed) contours indicate westerly (easterly) winds. **c,** Vertical profile of meridional wind response (110°E-130°E). **d,** 500hPa zonal wind changes (shading) and 500hPa temperature climatology (contours; interval = 2K from 265K). The thick green line in (c) indicates the latitudes of the target EA domain (green box in (d)), and the thick green lines in (d) denote longitudes east of Tibetan Plateau corresponding to (c).

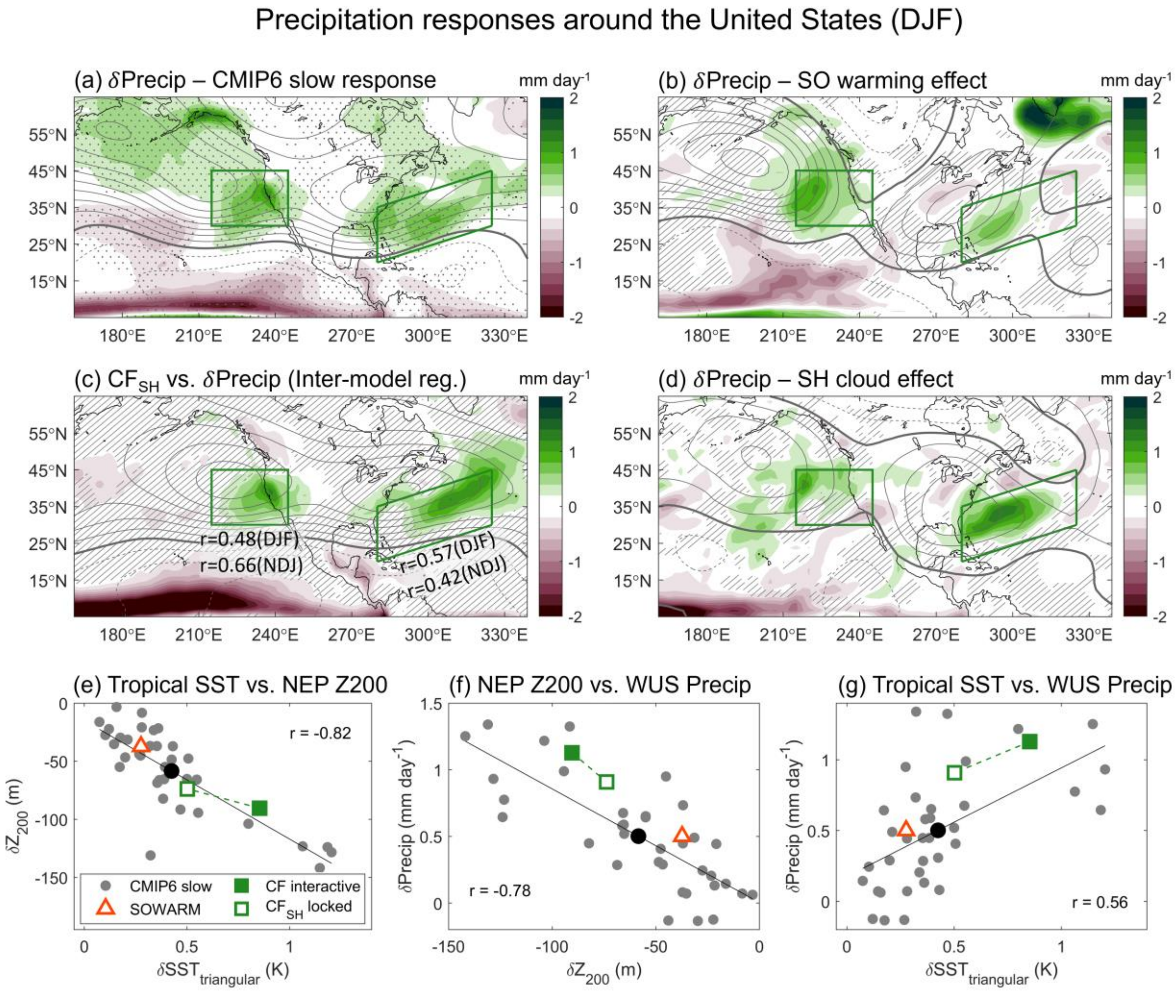

Fig. 4| Remote impact on the United States winter (DJF) precipitation. a-d, Precipitation (shading) and 200hPa geopotential height pattern (contours) from (**a**) the multi-model mean CMIP6 slow response, (**b**) the CESM1-CAM4 SO warming experiment, (**c**) the inter-model regression of CMIP6 slow response onto the CF_{SH}, and (**d**) the CESM1-CAM5 regional cloud locking experiment. The geopotential height pattern is calculated by subtracting the Northern Hemisphere average (0°-40°N) from the original value (Methods). The solid (dashed) gray contours represent negative (positive) anomalies (interval = 10m). Stippled and unhatched regions indicate the statistical significance, as in Figs. 1a-d. Green rectangle (parallelogram) corresponds to the regions for the WUS (SEUS) precipitation enhancement. **e-g,** Relationship between (**e**) the tropical Pacific triangular warming and northeastern Pacific 200hPa geopotential height anomaly, (**f**) the height anomaly and WUS precipitation enhancement, and (**g**) the triangular warming and WUS precipitation enhancement. The height anomalies are averaged over the northeastern Pacific between 30°N–55°N and 185°E–235°E. The symbols in (e-g) follow those in Figs. 2e-g.

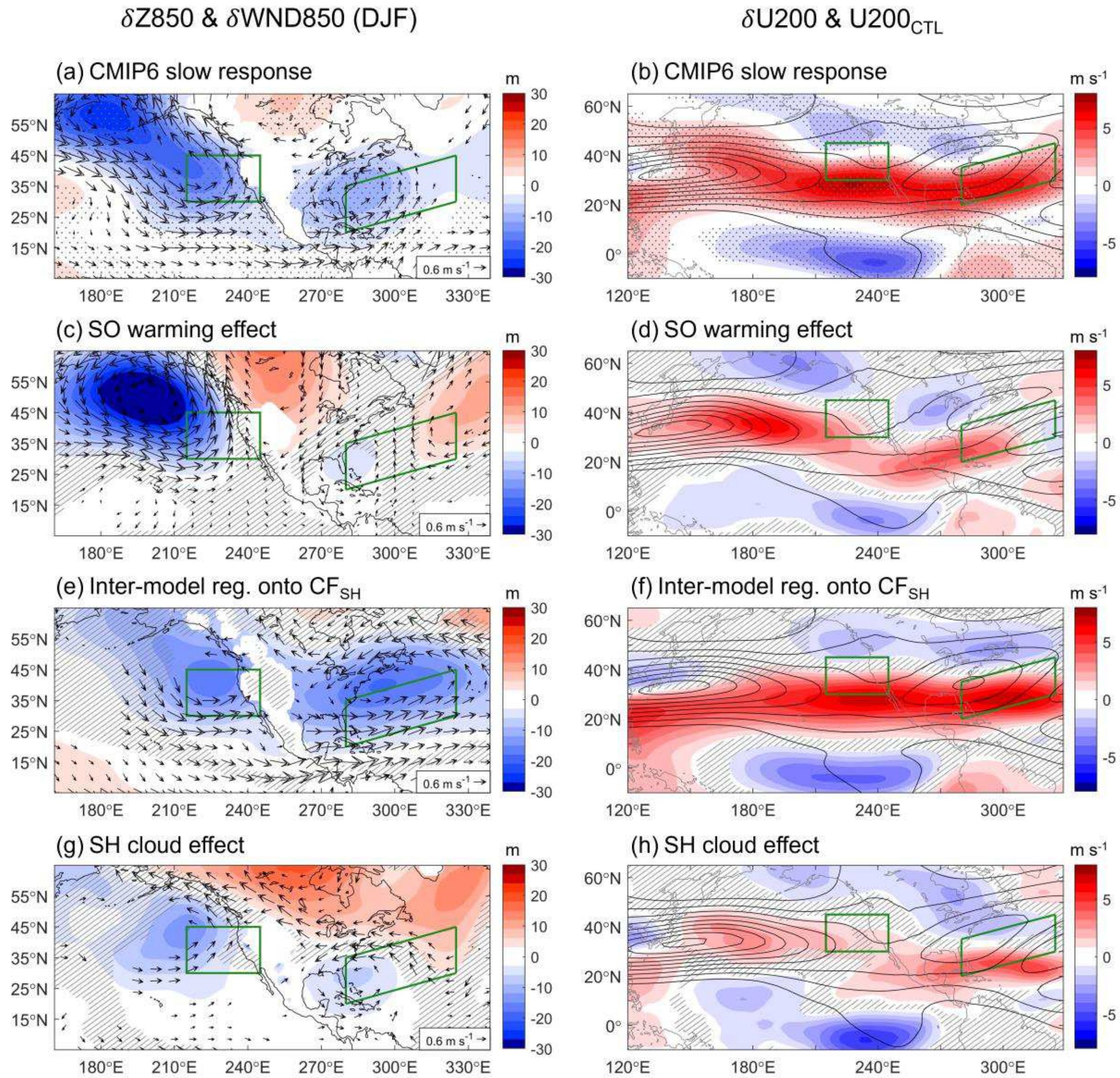

Fig. 5| The El Niño-like teleconnection to the Unites States. a,c,e,g, The 850hPa geopotential height pattern (shading) and 850hPa horizontal wind (vectors) from (**a**) the multi-model mean CMIP6 slow response, (**c**) the CESM1-CAM4 SO warming experiment, (**e**) the inter-model regression of CMIP6 slow response onto the CF_{SH}, and (**g**) CESM1-CAM5 regional cloud locking experiment. The vectors are shown if either the zonal or meridional component has robust sign of changes or statistically significant, following the significance metrics in Figs. 1a-d. **b,d,f,h**, same as a,c,e,g but for the changes (shading) and climatology (contours) of 200hPa zonal wind. Only the positive contours larger than 12 m s^{-1} are shown; the contour interval is 8 m s^{-1}. Green boxes indicate the Western and Southeastern United States, where precipitation increases.

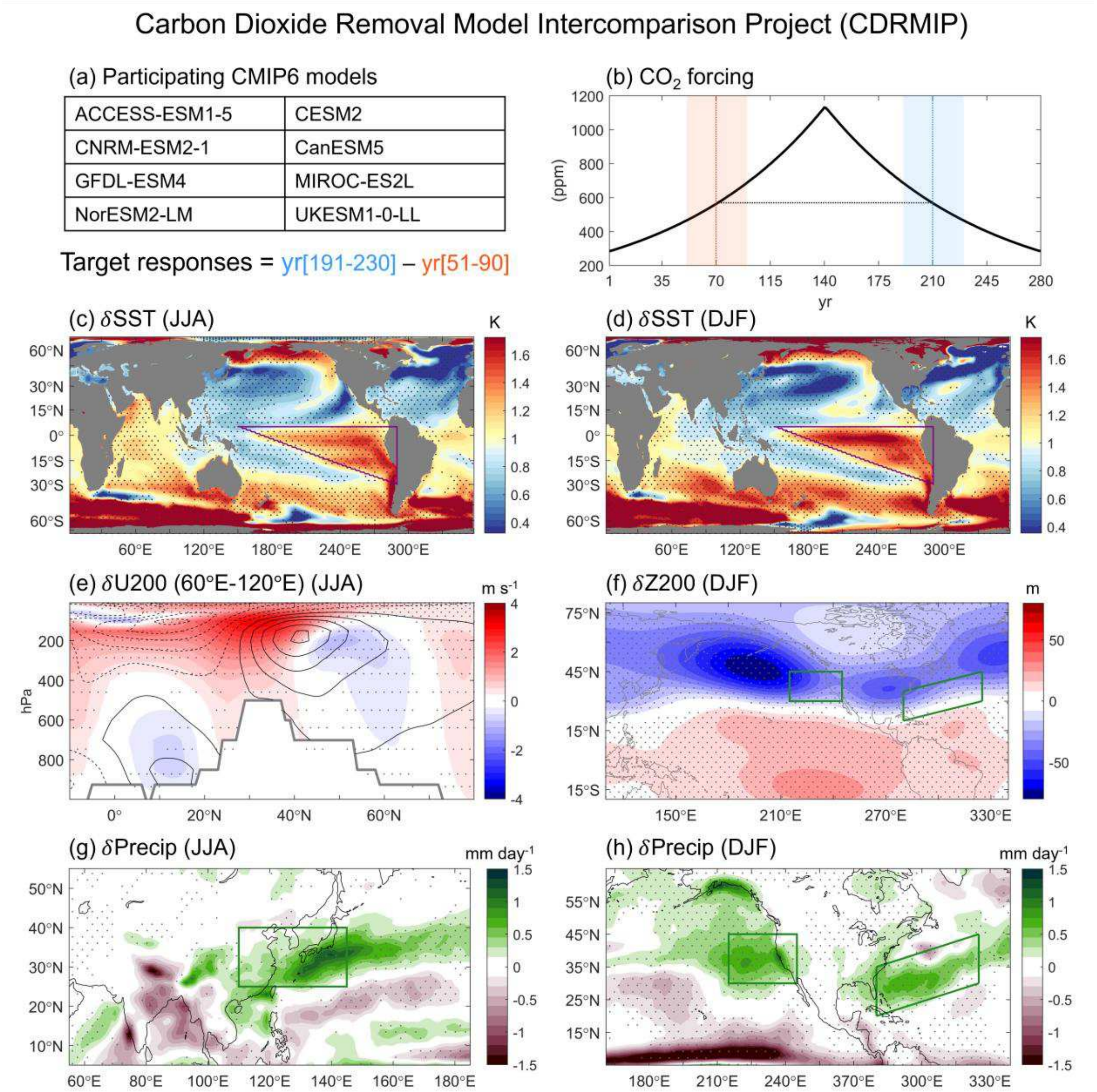

Fig. 6| Long-term persistent climate changes related to the Southern Ocean warming. a, Lists of CMIP6 models participating in the Carbon Dioxide Removal Model Intercomparison Project (CDRMIP)[8]. **b**, Transient CO_2 quadrupling and subsequent reduction used as the forcing in CDRMIP. The long-term persisting climate changes are measured by the difference between years 191-230 and 51-90 when CO_2 concentrations are identical. **c,d**, SST responses in (**c**) summer and (**d**) winter. **e**, Vertical profile of zonal wind changes in summer (shading) with corresponding climatology (contours; interval = 6 m s^{-1}). **f**, Responses in 200hPa geopotential height pattern during winter. **g,h**, Precipitation responses in (**g**) summer and (**h**) winter. Stippling indicates where >6 of 8 models agree on the sign of change. Green boxes are regions with precipitation enhancements investigated here.

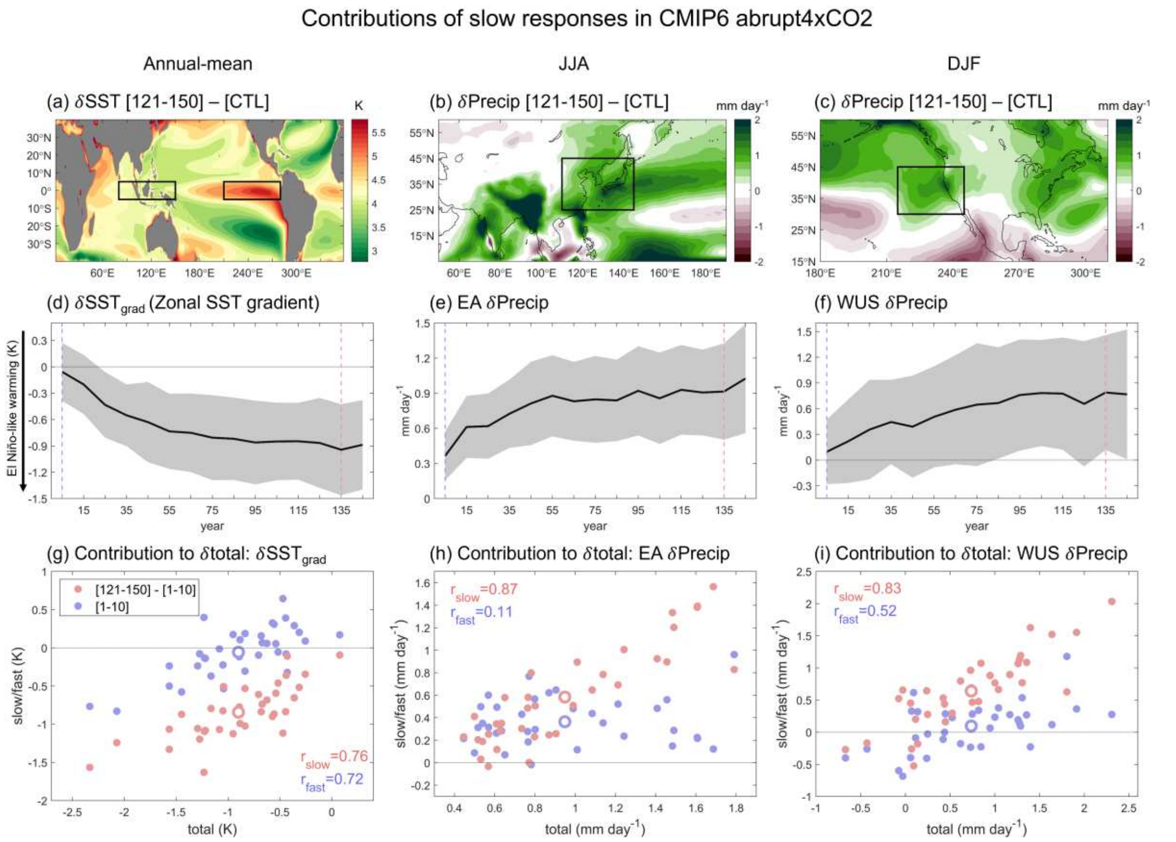

Extended Data Fig. 1| Contribution of slow response to the total response in CMIP6 CO_2 quadrupling simulation. Total response is difference between last 30 years of abrupt4xCO2 and last 100 years of pre-industrial control simulation, while slow response is difference between last 30 and first 10 years of abrupt4xCO2 simulation. Fast response is subtraction of the slow from the total response. **a-c**, Multi-model mean total response in **(a)** annual-mean SST, **(b)** summer precipitation, and **(c)** winter precipitation. **d-f**, Decadal averaged timeseries of the response in **(d)** equatorial Pacific SST gradient, precipitation over **(e)** East Asia and **(f)** the Western United States. The zonal SST gradient and regional precipitations are calculated over the black boxes in (a-c). Black lines represent multi-model mean and shading indicate $\pm$1 inter-model standard deviation. **g-i**, Total responses versus slow/fast responses for (g) equatorial Pacific SST gradient**,** precipitation over (h) East Asia and (i) the Western United States. For slow/fast response, inter-model correlation coefficients to the total response are inserted as text. Note that the definition of slow response–which uses first 10 years–is specific to this figure; in main analysis we use first 30 years to minimize the internal variability of the regional precipitation.

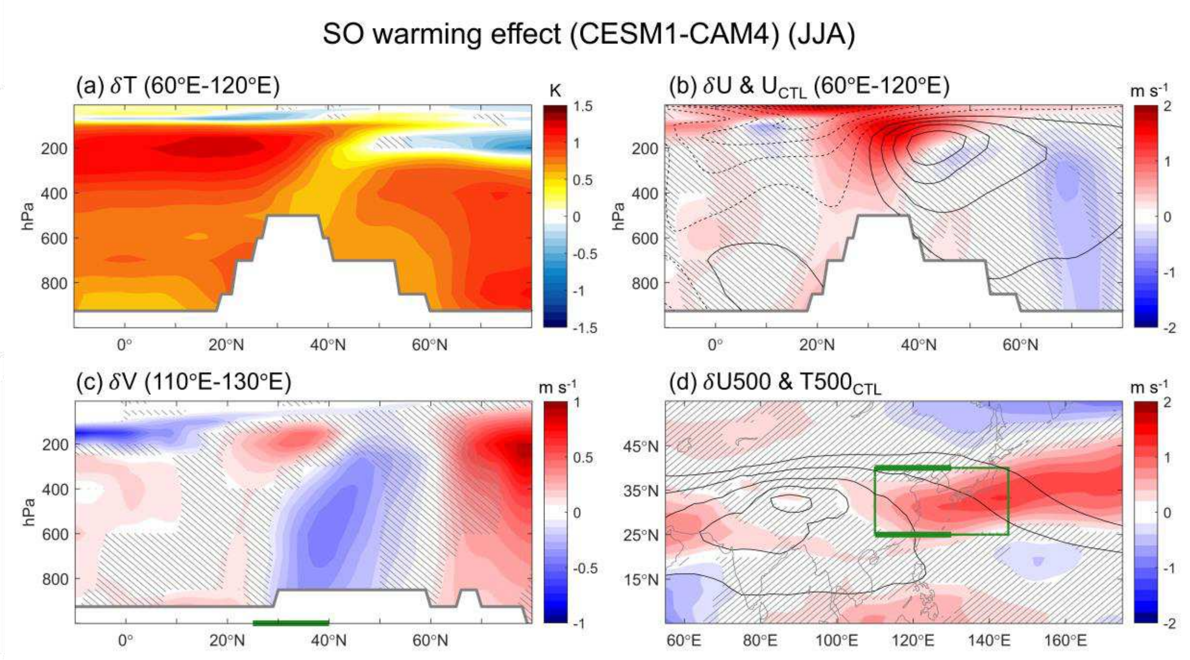

Extended Data Fig. 2| The El Niño-like teleconnection to East Asia in the SO warming experiment. a-d, same to Fig. 3 but for the CESM1-CAM4 SO warming experiment. Unhatched regions indicate statistically significant responses at the 95% level using a *t* test, compared to the inter-annual variability in control climate.

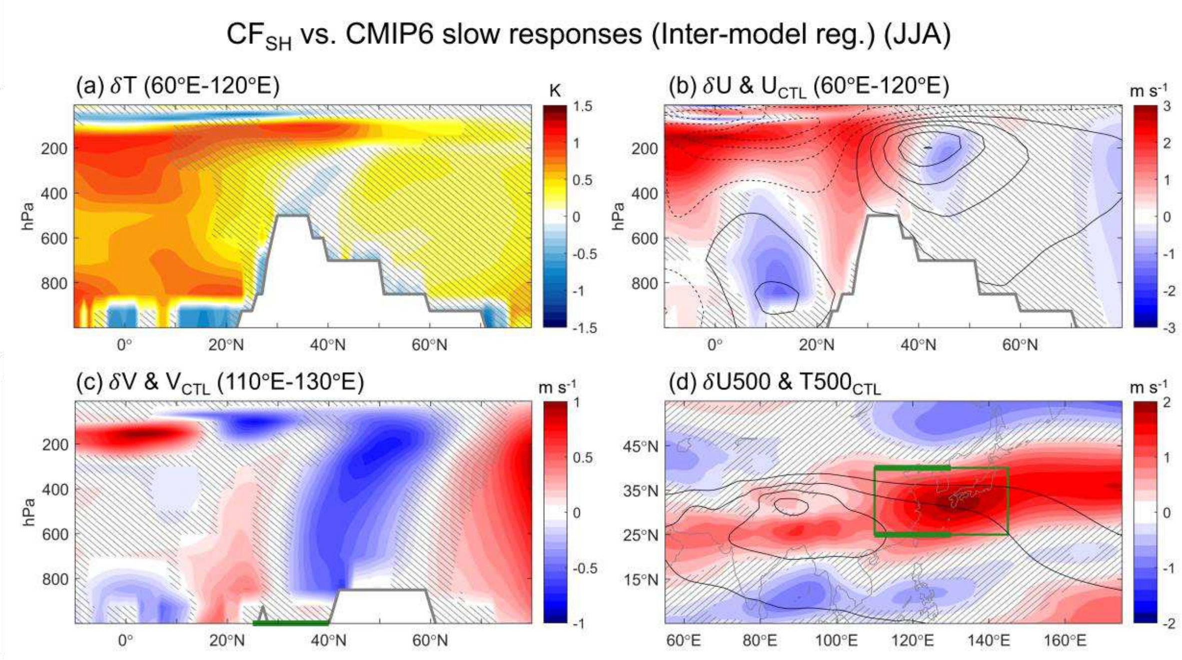

Extended Data Fig. 3| The El Niño-like teleconnection to East Asia for the CMIP6 inter-model regression. a-d, same to Fig. 3 but for the inter-model regression of CMIP6 slow response onto the CF_{SH}. Unhatched regions indicate statistically significant regression coefficients at the 95% level using a *t* test.

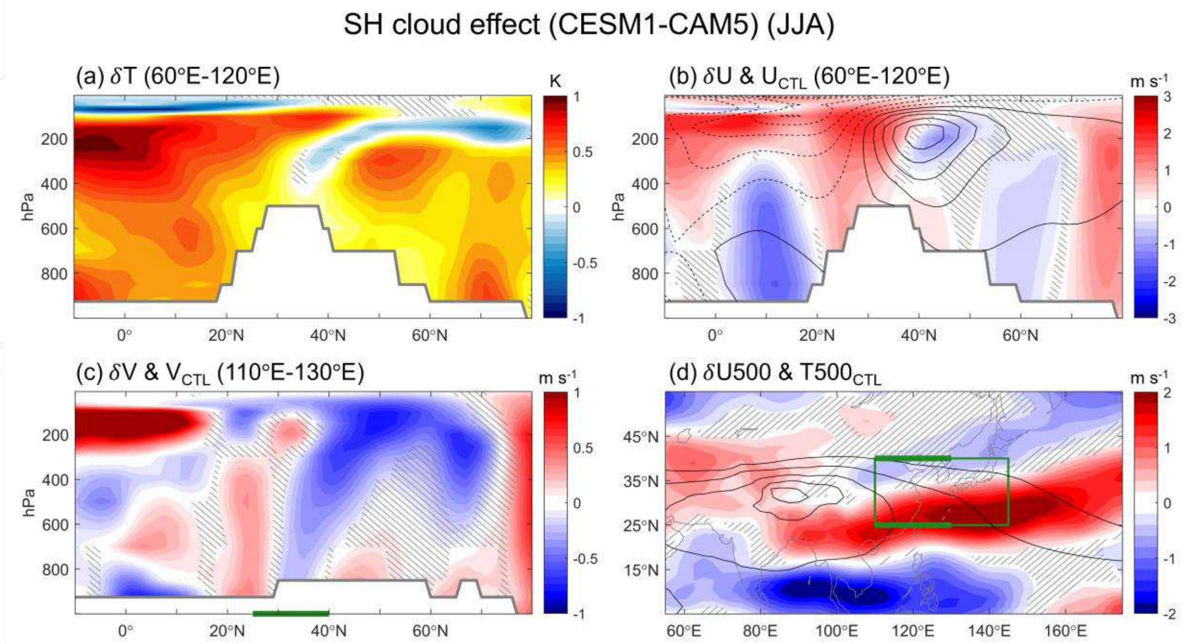

Extended Data Fig. 4| The El Niño-like teleconnection to East Asia in the cloud locking experiment. a-d, same to Fig. 3 but for the CESM1-CAM5 regional cloud locking experiment. Unhatched regions indicate statistically significant responses at the 95% level using a *t* test, compared to the inter-annual variability in control climate.

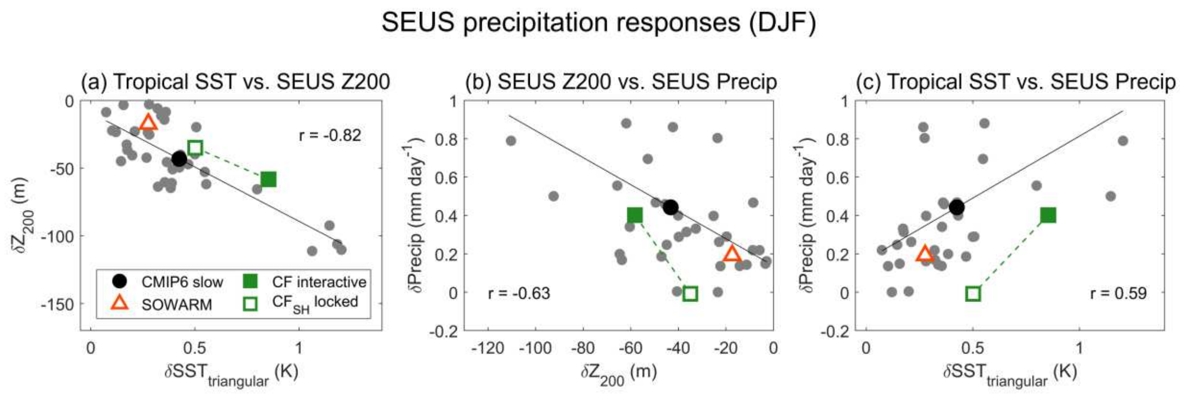

Extended Data Fig. 5| The El Niño-like teleconnection to the Southeastern Unites States. **a-c,** Winter (DJF) averaged relationship between (**a**) the tropical Pacific triangular warming and the 200hPa geopotential height anomalies over the SEUS, (**b**) the height anomalies and the SEUS precipitation enhancements, and (**c**) the triangular warmings and the precipitation enhancements. The 200hPa geopotential height anomalies are averaged for the SEUS between 25°–50°N and 260°–310°E. The SEUS precipitation is averaged over green parallelogram southeast of North America in Figs. 4a-d.

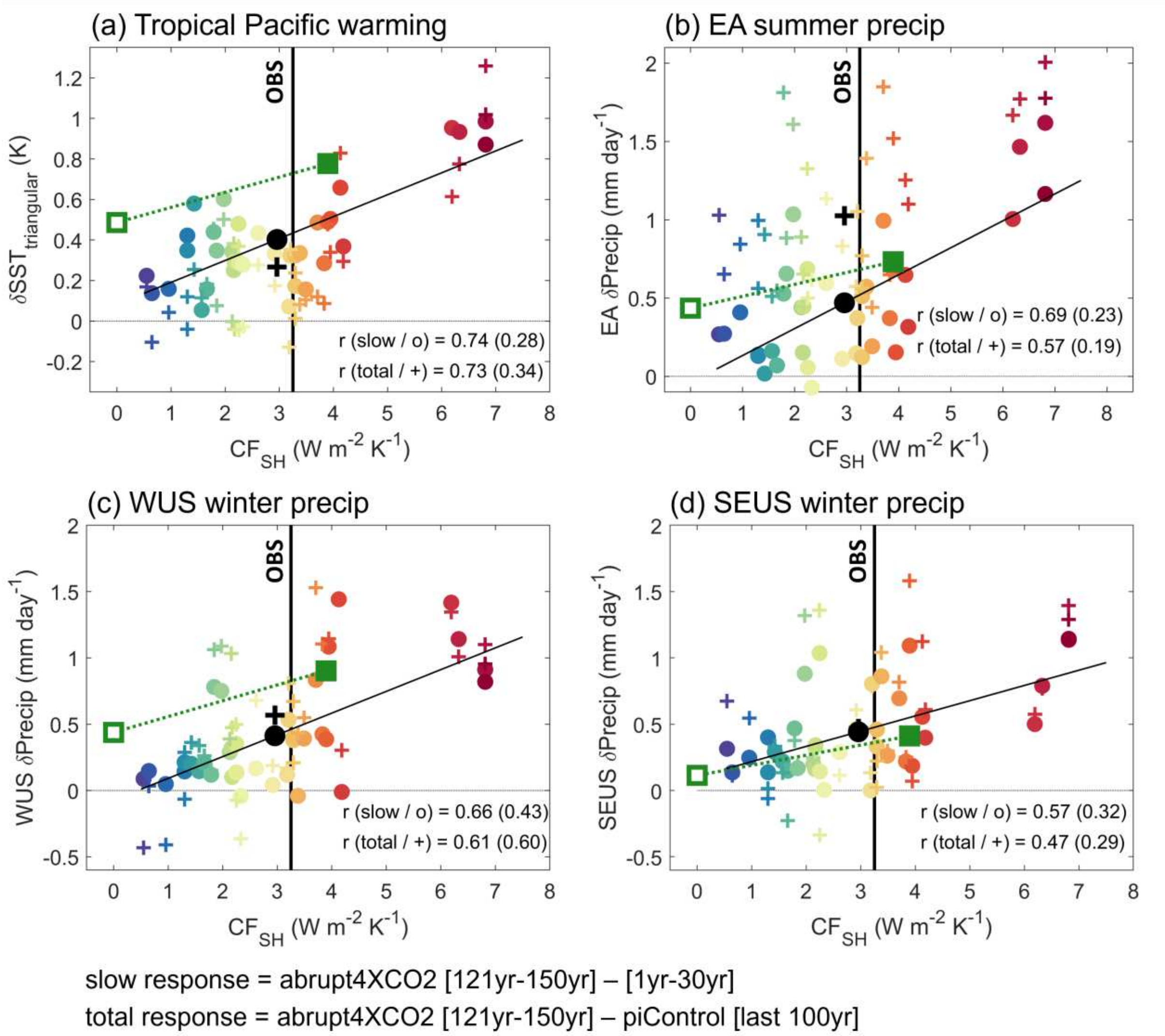

Extended Data Fig. 6| The role of the Southern Hemisphere low cloud feedback (CF$_{SH}$) on the future projection uncertainties. a-d, CF$_{SH}$ versus (**a**) the tropical Pacific triangular warming, the precipitation responses during the (**b**) EA summer, (c) WUS winter, and (**d**) SEUS winter. Circle (cross) symbols indicate CMIP6 slow (total) response. The inserted texts indicate inter-model correlation coefficients, where the values in parentheses are calculated after excluding four CESM2 variant models with the highest CF$_{SH}$ (Table S1). The symbols are color-coded from blue to red in ascending order of the CF$_{SH}$. Black symbol indicates muti-model mean and empty (filled) green rectangle indicates the CESM1-CAM5 experiment in which the clouds are regionally locked (globally interactive). The vertical black line indicates the observational estimate of CF$_{SH}$ (methods). Note that WUS winter is defined as November, December, January for CMIP6 slow response and as January, February, March for the cloud locking experiment, when each signal is maximized.

Supplementary Files

This is a list of supplementary files associated with this preprint. Click to download.

- suppfinal.pdf